Journal of Power Sources 528 (2022) 231177

Contents lists available at ScienceDirect

Journal of Power Sources

journal homepage: www.elsevier.com/locate/jpowsour

Modeling the effect of electrolyte microstructure on conductivity and solid-state Li-ion battery performance

Maya Horii [a,1], Rebecca J. Christianson [b], Heena Mutha [b,2], John Christopher Bachman [a,*]

[a] Department of Mechanical Engineering, California State University, Los Angeles, Los Angeles, CA, 90032, United States
[b] The Charles Stark Draper Laboratory, Inc., Cambridge, MA, 02139, United States

HIGHLIGHTS

- A resistor network model and battery performance model were combined.
- Effects of electrolyte microstructure on Li-ion battery performance were studied.
- Design rules were found for an Al-LLZO electrolyte in a Li .|| $LiCoO_2$ battery.
- Electrolyte conductivity ratio to thickness above 10 S m^{-2} is needed at C-rates>10.
- Diminishing returns predicted from further improvement of Al-LLZO conductivity.

ARTICLE INFO

Keywords:
Solid-state battery
Solid electrolyte
Microstructure
Battery modeling
Lithium-ion battery
Energy storage

ABSTRACT

Solid-state batteries offer the potential to improve safety, cyclability, and energy density of Li-ion batteries. However, their conductivity, stability, and processing limit their use. To this end, the effects of solid electrolyte microstructure on overall battery performance are determined. The conductivities of Al-doped $Li_7La_3Zr_2O_{12}$ (Al-LLZO), with a range of microstructures, are found using a resistor network model. Varying electrolyte properties are combined with a Li-metal negative electrode and $LiCoO_2$ positive electrode in a 1-D continuum model to predict the effects on performance. Simulations suggest that the ratio of electrolyte conductivity to electrolyte thickness must remain above 10 S m^{-2} to maintain high energy and power output, particularly at C-rates greater than 10. To maintain conductivity near the grain interior conductivity, a grain size at least 10,000 times larger than grain boundary thickness is needed. Further improvements in grain size, grain boundary thickness, and void fraction beyond typical Al-LLZO microstructures, with the goal of higher conductivities, are predicted to have diminishing returns in overall battery performance, even at more sensitive high C-rates up to 100.

1. Introduction

Li-ion batteries are the prefered power source for a large range of technologies including grid storage, electric vehicles, mobile phones, and sensors. Conventionally, these batteries contain a liquid electrolyte, which is flammable and can leak [1]. By replacing liquid electrolytes with solid electrolytes, these issues can be addressed. Solid electrolytes can also provide increased chemical stability, high Li-ion transference numbers (~1), and enable the use of energy-dense Li metal by providing a mechanical barrier to dendrite formation [2,3]. Currently, some promising materials for solid-state electrolytes include oxides with garnet structures, perovskites, and sodium superionic conductors (NASICONs) [3,4]. This paper focuses on the modeling of Al-LLZO systems. LLZO ($Li_7La_3Zr_2O_{12}$) has emerged as an excellent solid electrolyte due to its high Li-ion conductivity, low electronic conductivity, and wide electrochemical stability window [5–7]. When doped with Al, the highly conductive cubic phase of LLZO (as opposed to the less conductive tetragonal phase) becomes stable at room temperature and can be synthesized at a low sintering temperature [5,8]. In its tetragonal phase (space group no. 142, $I4_1/acd$), Li sites are fully occupied, whereas Li sites are only partially occupied in the cubic phase (space group no. 230, $Ia\bar{3}d$), causing higher Li mobility and conductivity [9,10]. Though the

---

* Corresponding author.
E-mail address: john.bachman@calstatela.edu (J.C. Bachman).
[1] Present address: Department of Mechanical Engineering, University of California, Berkeley, Berkeley, CA 94720, United States.
[2] Present address: Commonwealth Fusion Systems, Cambridge, MA 02139, United States.

https://doi.org/10.1016/j.jpowsour.2022.231177
Received 7 December 2021; Received in revised form 10 February 2022; Accepted 12 February 2022

local structure of doped cubic LLZO has been a recent focus of study, the exact crystallographic structure of Al dopants is still not fully understood [11]. An example of the Al-LLZO crystal structure can be found in the Supplementary Information (Fig. S1) [8]. Overall, Al-LLZO has been found to have conductivities up to 4×10^{-4} S cm^{-1} [8]. Additionally, Al doping can improve densification during sintering [12].

Some challenges in the development of solid-state batteries include poor interfacial connectivity, which can cause high resistances (10^2–10^3 Ω cm^2) and be exacerbated by delamination during cycling due to electrode volume changes, especially with stiff electrolytes [2,5,13]. Additionally, though solid electrolytes provide greater protection against dendrite growth than conventional liquid electrolytes, there are still issues with dendrite growth in solid-state systems [14–16]. The manufacturing and processing of solid-state batteries also poses a challenge. To realize the high energy density of solid-state batteries, their electrolytes must be extremely thin (≤100 μm) to reduce excess resistance, volume, and weight [17]. The manufacturing of these thin-film solid electrolytes, especially at a competitive price, is a significant obstacle to commercial solid-state battery use [17]. Despite these challenges, they are a promising technology to improve the safety and longevity of batteries in the future [2,17].

To match the performance of conventional Li-ion batteries, solid electrolytes must be able to conduct Li ions with an ionic conductivity of at least 10^{-4} S cm^{-1} [1,18]. The overall conductivity of a solid electrolyte is affected by both the grain boundary and grain interior conductivities. Consequently, there has been significant investigation of the relationship between the microstructure and ionic conductivity of common solid-state electrolytes, including LLZO, both experimentally and through modeling [19–22]. Previous work has characterized the microstructure and the different ionic conductivity contributions of grain boundaries and grain interiors in Al-LLZO [23], finding higher ionic conductivity in grain interiors [6]. The effect of varying the grain size and relative density of LLZO on its ionic conductivity has been experimentally studied as well, with results that suggest increased ionic conductivity with larger grain sizes and higher relative densities [24,25].

Solid-electrolyte microstructure can be altered through variations in processing methods. Currently, solid-state reactions, sol-gel methods, field-assisted sintering, and coprecipitation, are some of the main methods used to synthesize LLZO [26]. Solid-state reactions are the most common and are advantageous due to their simplicity and low cost [26]. Al-LLZO has been synthesized through solid-state reactions with conductivities up to 4.4×10^{-4} S cm^{-1}, while Ga-LLZO has reached conductivities up to 1.46×10^{-3} S cm^{-1} [26]. It has also produced electrolytes with high relative densities up to 99% [24] and grain sizes up to ~200 μm [27]. Additionally, grain boundary thicknesses around 2–7.5 nm have been found for Al-LLZO, indicating that the grain boundary is a region of relative disorder between grains consisting of many atomic layers [23,28–30]. Using field-assisted sintering technology, which is beneficial for its short sintering time, Al-LLZO electrolytes have been manufactured with up to 5.7×10^{-4} S cm^{-1} conductivities, relative densities of 99.8%, and grain sizes of 10 μm [26,31]. Factors such as initial powder particle size, temperature, time of sintering, and pressure can be used to manipulate the microstructure of LLZO [24,27,32,33].

Pulsed laser deposition, sputtering, and sol-gel methods in particular have also been used to create thin-film LLZO electrolytes [34–36]. Estimations have found that LLZO electrolytes with conductivities within 10^{-4}-10^{-3} S cm^{-1} must have thicknesses below ~4 μm to match the resistance of traditional electrolytes, indicating the importance of both high conductivities and thin-film manufacturing methods [37]. Thin-film LLZO electrolytes have been created with conductivities up to 6.36×10^{-4} S cm^{-1} [22] and grain sizes have been measured between 50 nm and 100 nm for electrolytes less than 1.5 μm thick [22,35].

Through modeling, researchers have investigated the relationship between microstructure and ionic conductivity in solid electrolytes using techniques including: molecular dynamics simulations [38–41], equivalent circuit models [40], finite element analysis [42,43], and resistor network models [42]. Additionally, many models simulating solid-state Li-ion battery performance have been created and experimentally validated [44–50]. Many of these models track Li movement by simulating diffusion and migration throughout the battery, allowing for calculation of overpotential losses and overall voltage [44,49,50]. Some models are able to account for the effects of temperature, heat transfer and heat generation within the battery, and varying diffusion coefficients. However, there is no systematic computational investigation of the effects of solid electrolyte grain structure on overall battery performance to the authors' knowledge.

This paper describes a resistor network model able to predict the conductivity and diffusion coefficient of Al-LLZO based on grain size, grain boundary thickness, and void density. This is coupled with a continuum, 1-D, finite-difference model to predict the battery performance during discharge. Together, these models are used to characterize the effect of Al-LLZO microstructure on the performance of a battery system with a Li-metal anode, a solid-state Al-LLZO electrolyte, and a LiCoO$_2$ cathode.

2. Experimental

To determine the effect of Al-LLZO grain structure on battery performance, a resistor network model and battery model were developed. The symbols used in this model are shown in Table 1.

Common methods of modeling resistance and conductivity are layer models, such as the brick layer model, or effective medium theory models, such as the Maxwell-Wagner model [51]. The resistor network model was chosen instead for its simplicity and ability to model multi-directional current flow, unlike the brick layer model. This is particularly important in modeling non-homogenous microstructures, such as a structure with randomly placed voids, where the preferred current path may not be a straight line [52,53]. This enables resistor network models to calculate conductivity with good accuracy within the given geometries [42].

A schematic representation of the model is presented in Fig. 1a. Grain structure is represented using 2-D squares as grain shapes, where the outline of each grain represents a grain boundary. Each element (grain, grain boundary segment) is represented using four resistors arranged in a cross-shape, as shown in Fig. 1b. In the square grain interior, each resistor represents an equal current path length along an equally conductive material and therefore has the same resistance in each direction. However, the grain boundaries are segmented into elements surrounding the grains, which can be rectangular and have resistors representing different path lengths. One set of resistors in the grain boundary have the resistance $R_{GB,shortpath}$, which represents the resistance along half of the thickness of the grain boundary (the short path), while a second set of resistors have the resistance $R_{GB,longpath}$, representing the resistance along half of the length of the grain (the long path). The grain interior and grain boundaries can be further segmented into smaller elements to create a denser mesh or to add varied grain or void sizes. By using resistors instead of conductors, as is done in Refs. [54,55], the vastly different scales of grain boundary thickness and grain size can easily be represented using a minimal number of nodes.

To calculate the value of the resistances $R_{GB,longpath}$, $R_{GB,shortpath}$, and R_{GI}, the relationship between conductivity and resistance is used.

$$R = \frac{L_R}{\sigma A_R} \tag{1}$$

Where L_R is the length of the resistor, σ is the conductivity of the material, and A_R is the area the current passes through. The area is calculated by assuming a constant thickness h in Fig. 1.

$$R_{GB,longpath} = \frac{L_{GI}}{2\sigma_{GB}A_R} = \frac{L_{GI}}{2\sigma_{GB}L_{GB}h} \tag{2}$$

Table 1
Symbols used in model.

Symbol	Parameter	Unit
A	Cross-sectional area	m^{2}
A_R	Area of resistor	m^{2}
$a(y,t)$	Equal to a_{Li^+} and a_{n^-} under electroneutrality	mol m^{-3}
a_{n^-}	Activity of negative charge carrier in the electrolyte	mol m^{-3}
a_0	Initial activity of Li in the electrolyte	mol m^{-3}
a_j	Activity of species j	mol m^{-3}
a_{Li^+}	Activity of mobile Li ions in the electrolyte	mol m^{-3}
a_{Li^0}	Activity of immobile Li in the electrolyte	mol m^{-3}
$a^0_{LiCoO_2}$	Initial activity of Li in the positive electrode	mol m^{-3}
a_{LiCoO_2}	Activity of Li in the positive electrode	mol m^{-3}
D_j	Diffusion coefficient of species j	m^{2} s^{-1}
D_{Li}	Diffusion coefficient of Li in the positive electrode	m^{2} s^{-1}
D_{Li+}	Diffusion coefficient of Li$^+$ in the electrolyte	m^{2} s^{-1}
D_{n-}	Diffusion coefficient of negative charge carrier in the electrolyte	m^{2} s^{-1}
e	Elementary charge	C
E	Electric field	V m^{-1}
E^{eq}_{bat}	Equilibrium battery voltage	V
E_{bat}	Battery voltage	V
$E^{eq}_{LiCoO_2}$	Equilibrium voltage of the positive electrode	V
F	Faraday's constant	As mol^{-1}
h	Thickness of material in resistor network model	m
I	Current in battery	A
$I^0_{LiCoO_2}$	Exchange current in the positive electrode	A
I_{LiCoO_2}	Current in the positive electrode	A
J_j	Ionic flux of species j	mol m^{-2} s^{-1}
k	Number of iterations in successive overrelaxation	–
k_B	Boltzmann constant	J K^{-1}
k_d	Rate constant for Li-ion generation reaction in the electrolyte	s^{-1}
k_{pos}	Standard rate constant for positive electrode charge transfer reaction	m$^{2.8}$ mol$^{-0.6}$ s^{-1}
k_r	Li-ion recombination rate in the electrolyte	m^{3} mol^{-1} s^{-1}
L	Length of electrolyte	m
L_{GB}	Grain boundary thickness	m
L_{GI}	Grain size	m
L_R	Length of resistor	m
M	Thickness of positive electrode	m
n	Density of mobile ions	m^{-3}
R	Gas constant	J mol^{-1} K^{-1}
r	Rate of regeneration and recombination of mobile Li ions in the electrolyte	mol s^{-1}
$R_{GB,longpath}$	Resistance representing the longer dimension in a grain boundary	Ω
$R_{GB,shortpath}$	Resistance representing the shorter dimension in a grain boundary	Ω
R_{GI}	Resistance of grain interior	Ω
R_{ij}	Combined resistance between node i and j	Ω
T	Temperature	K
t	Time	s
t_+	Ionic transference number of Li ions in the electrolyte	–
V^k_i	Voltage at node i, iteration k	V
V_i	Voltage at node i	V
V_j	Voltage at node j adjacent to node i	V
x^s	Normalized Li activity at the positive electrode surface	–
$\overline{x}$	Average normalized Li activity in the positive electrode	–
y	Coordinate system in battery performance model	m
z_j	Valence of species j	–
α_{LiCoO_2}	Charge transfer coefficient for positive electrode	–
η_{ct}	Charge transfer overpotential	V
η_d	Diffusion overpotential	V
η_r	Resistance overpotential	V
η_{total}	Total overpotential	V
$\sigma_{GB\ Total}$	Total grain boundary contribution to conductivity	S m^{-1}
σ_{GB}	Specific grain boundary conductivity of Al-LLZO	S m^{-1}
σ_{GI}	Grain interior conductivity of Al-LLZO	S m^{-1}
δ	Fraction of mobile lithium in the electrolyte at equilibrium	–
σ	Conductivity	S m^{-1}
ω	Relaxation parameter	–

$$R_{GB,shortpath} = \frac{L_{GB}}{2\sigma_{GB}A_R} = \frac{L_{GB}}{2\sigma_{GB}L_{GI}h} \tag{3}$$

$$R_{GI} = \frac{L_{GI}}{2\sigma_{GI}A_R} = \frac{L_{GI}}{2\sigma_{GI}L_{GI}h} = \frac{1}{2\sigma_{GI}h} \tag{4}$$

Using Kirchoff's law to sum the current entering each node, the voltage throughout the material can be determined [54,55].

$$\sum_j \frac{(V_i - V_j)}{R_{ij}} = 0$$

$$V_i = \frac{\sum_j \frac{V_j}{R_{ij}}}{\sum_j \frac{1}{R_{ij}}} \tag{5}$$

In Equation (5), V_i represents the voltage of node i, V_j represents the voltage of nodes j which are directly connected to node i, and R_{ij} represents the combined resistance between node i and node j. To solve for the voltage of each node in the matrix, an iterative solving process is used. The successive overrelaxation method is applied in order to increase the speed of convergence [54–56].

$$V_i^{k+1} = (1-\omega) * V_i^k + \omega \frac{\sum_j \frac{V_j}{R_{ij}}}{\sum_j \frac{1}{R_{ij}}} \tag{6}$$

In Equation (6), k represents the number of iterations and ω is the relaxation parameter. A voltage was imposed at opposite sides of the node matrix, with one edge at 1 V and the opposite at 2 V. Then, the total current simulated through the matrix was determined, allowing the resistance of the material to be calculated. The material is assumed to have homogenous resistance for purposes of the battery modeling.

Once the conductivity is determined, the Nernst-Einstein equation is used to determine the diffusion coefficient of Li ions in the electrolyte.

$$D = \sigma \frac{k_B T}{n(ze)^2} \tag{7}$$

In this equation, D is the diffusion coefficient of Li ions, σ is the conductivity of Li ions, k_B is the Boltzmann constant, T is the temperature, n is the density of mobile ions, z is the valence, and e is the elementary charge [57].

The negative ion diffusion coefficient, D_-, in the electrolyte is determined using the following equation in combination with the transference number of the positive ion (Li$^+$), t_+, and the positive ion diffusion coefficient in the electrolyte, D_+ [58].

$$t_+ = \frac{D_+}{D_+ + D_-} \tag{8}$$

The electrolyte model was integrated into a device model to calculate battery voltage over time. The battery described is a solid-state battery with a Li-metal electrode, a $LiCoO_2$ electrode, and an Al-LLZO electrolyte. The battery reactions at the positive and negative electrodes, depicted in Fig. 2, are described in Equations (9) and (10) respectively.

$$LiCoO_2 \rightleftarrows Li_{1-x}CoO_2 + xLi^+ + xe^- \quad (0 \le x \le 0.5) \tag{9}$$

$$Li \rightleftarrows Li^+ + e^- \tag{10}$$

To track Li ions through space and time, the Nernst-Plank equation is used, defined as

$$J_j = -D_j \frac{\partial a_j}{\partial y} + \frac{z_j F}{RT} D_j a_j E \tag{11}$$

where J_j represents the ionic flux of the species j (either Li ions or $La_3Zr_2O_{12}$ negative ions), D_j represents the diffusion coefficient of the species j, a_j represents the activity of the species j, y represents distance, E represents the potential gradient, z_j represents the valence of species j, and T is the temperature of the battery [44]:

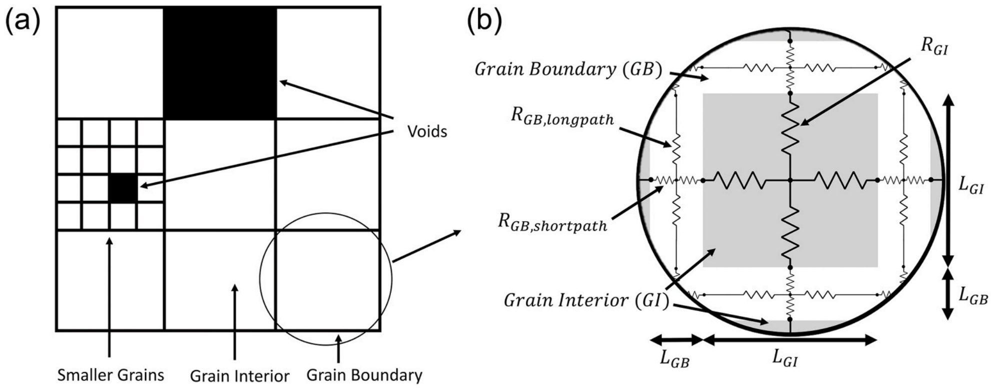

Fig. 1. (a) Schematic of grain structure model showing various grain sizes (white squares), grain boundaries (black lines), and voids (black squares). (b) Schematic of resistor network model showing one grain interior node with four resistors and four grain boundary nodes with four resistors whose length depends on the node location.

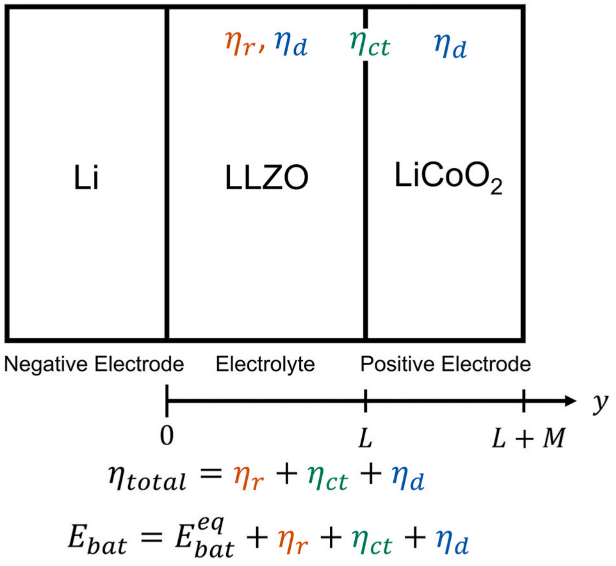

Fig. 2. Schematic of solid-state Li-ion battery with overpotentials associated with resistance in the electrolyte (η_r), diffusion in the electrolyte and positive electrode (η_d), and charge transfer at the interface (η_{ct}).

The rate of regeneration and recombination of mobile Li ions in the electrolyte, r, is defined as

$$r = k_d a_{Li^0} - k_r a_{Li^+} a_{n^-} \tag{12}$$

Where k_d is the rate constant for the ionic generation reaction ($k_d = k_r a_0 \delta^2/(1-\delta)$), k_r is the rate constant for the ionic recombination reaction, a_{Li^0} represents the activity of immobile Li in the electrolyte, a_{Li^+} represents the activity of mobile Li ions in the electrolyte, and a_{n^-} represents the activity of negative charge carrier in the electrolyte [44].

Equations (13)–(16) are derived under the assumption of no side reactions and electroneutrality defined by $a(y,t) = a_{n^-}(y,t) = a_{Li^+}(y,t)$ [44].

$$\frac{\partial a}{\partial t} = \frac{2D_{Li+}D_{n-}}{D_{Li+}+D_{n-}}\frac{\partial^2 a}{\partial y^2} + r \tag{13}$$

$$a(y,\ 0) = \delta a_0 \tag{14}$$

$$\frac{\partial a(0,t)}{\partial y} = \frac{I}{2FAD_{Li+}} \tag{15}$$

$$\frac{\partial a(L,t)}{\partial y} = \frac{I}{2FAD_{Li+}} \tag{16}$$

In Equations (13)–(16), n^- represents negative charge carrier, L represents the length of the electrolyte, t represents time, δ represents the fraction of Li ions that are mobile at equilibrium, and a_0 represents the total activity of Li ions in the electrolyte. Equation (13) represents the behavior in the bulk of the electrolyte, Equation (14) represents the initial condition of the electrolyte, and Equations (15) and (16) represent the boundary conditions. A similar derivation can be performed for the positive electrode, assuming no migration and a constant diffusion coefficient [44].

$$\frac{\partial a_{LiCoO_2}}{\partial t} = D_{Li}\frac{\partial^2 a_{LiCoO_2}}{\partial y^2} \tag{17}$$

$$a_{LiCoO_2}(y,0) = a^0_{LiCoO_2} \tag{18}$$

$$D_{Li}\frac{\partial a_{LiCoO_2}(L,t)}{\partial y} = \frac{I(t)}{FA} \tag{19}$$

$$D_{Li}\frac{\partial a_{LiCoO_2}(L+M,t)}{\partial y} = 0 \tag{20}$$

In Equations (17)–(20), M represents the length of the positive electrode and a_{LiCoO2} represents the activity of Li in the positive electrode. Equation (17) represents the behavior in the bulk of the electrode, Equation (18) represents the initial condition of the electrode, and Equations (19) and (20) represent the boundary conditions. The equations governing Li-ion diffusion are discretized, and the finite difference method is used to calculate activities at nodes through space and time.

Using information about Li distribution throughout the battery model, overpotentials within the battery are calculated. The first overpotential component is the resistance overpotential, η_r, in the electrolyte. This is calculated using the following equations, where the electric field solution is determined under the electroneutrality assumption, where $a(y,t) = a_{n^-}(y,t) = a_{Li^+}(y,t)$ [44].

$$\eta_r(t) = -\int_0^L E(y,t)dy \tag{21}$$

$$E(y,t) = \frac{RT}{F}\frac{1}{a(y,t)}\left[\frac{-I}{2FAD_{Li+}} + \frac{D_{Li+}-D_{n-}}{D_{Li+}+D_{n-}}\left(\frac{\partial a(y,t)}{\partial y} - \frac{I}{2FAD_{Li+}}\right)\right] \tag{22}$$

Next, the charge transfer overpotential (η_{ct}) is calculated using the Butler-Volmer relationship [44]:

$$I_{LiCoO_2} = I^0_{LiCoO_2}\left[\exp\left(\alpha_{LiCoO_2}\left(\frac{F}{RT}\right)\eta_{ct}\right) - \exp\left(\left(\alpha_{LiCoO_2} - 1\right)\left(\frac{F}{RT}\right)\eta_{ct}\right)\right] \tag{23}$$

In this equation, α_j represents the charge transfer coefficient of species j, I_{LiCoO_2} represents the current, and $I^0_{LiCoO_2}$ represents the exchange current. Under the assumption of no side reactions, I_{LiCoO_2} is assumed to be equal to I. The exchange current is defined as follows [59]:

$$I^0_{LiCoO2} = Fk_{pos}\left(\frac{\left(a_{LiCoO_2,max} - a_{LiCoO_2}(L,t)\right)a_{Li^+}(L,t)}{\left(a_{LiCoO_2,max} - a_{LiCoO_2,\,min}\right)a_0}\right)^{\alpha_{LiCoO_2}}\left(\frac{\left(a_{LiCoO_2}(L,t) - a_{LiCoO_2,\,min}\right)}{\left(a_{LiCoO_2,max} - a_{LiCoO_2,\,min}\right)}\right)^{1-\alpha_{LiCoO_2}} \tag{24}$$

k_{pos} represents the standard rate constant of the reaction, $a_{LiCoO_2,max}$ and $a_{LiCoO_2,min}$ represent the maximum and minimum respective lithium activities in the positive electrode. Lastly, the diffusion overpotential in the positive electrode and electrolyte, η_d, is calculated.

$$\eta_d = E^{eq}_{LiCoO_2}(x^s) - E^{eq}_{LiCoO_2}(\overline{x}) + \frac{RT}{F}\ln\left(\frac{a_{Li^+}(L,t)}{a_{Li^+}(0,t)}\right) \tag{25}$$

η_d represents the deviation from the standard potential given by the Nernst equation, with the first two terms reflecting the contributions of the positive electrode, and the last term representing contributions of the electrolyte [59]. x^s and $\overline{x}$ are Li activities normalized by $a_{LiCoO_2,max}$ where x^s represents normalized surface activity and $\overline{x}$ represents normalized average activity in the positive electrode. To calculate $E^{eq}_{LiCoO_2}$, the equilibrium voltage of the positive electrode, experimentally determined values which describe the equilibrium voltage as a function of lithiation are used [59]. The right-hand term of the overpotential equation describes the contribution of electrolyte Li activities to the Nernst equation.

Table 2
Parameters used within model (values at room temperature, 25 °C).

Symbol	Parameter	Value	Reference
α_{LiCoO_2}	Charge transfer coefficient for positive electrode	0.6	[44]
A	Cross-sectional area	1×10^{-4} m^2	
D_{Li}	Diffusion coefficient of Li in the positive electrode	1.76×10^{-15} m^2 s^{-1}	[44]
δ	Fraction of mobile lithium in the electrolyte at equilibrium	0.8	[8]
L_{GB}	Grain boundary thickness in Al-LLZO[a]	7.5×10^{-9} m	[23]
σ_{GI}	Grain interior conductivity of Al-LLZO	7.7×10^{-2} S m^{-1}	[60]
L_{GI}	Grain size in LLZO[a]	1×10^{-7} m	[35]
a_0	Initial activity of Li in the electrolyte	39925.03 mol m^{-3}	
$a^0_{LiCoO_2}$	Initial activity of Li in the positive electrode	21045.06 mol m^{-3}	
t_+	Ionic transference number of Li ions in the electrolyte	0.9999998	[8]
M	Length of the electrode	5×10^{-7} m	
L	Length of the electrolyte[a]	1×10^{-5} m	
k_r	Li-ion recombination rate in the electrolyte	0.9×10^{-8} m^3 mol^{-1} s^{-1}	[44]
$a_{LiCoO_2,max}$	Maximum activity of Li in the positive electrode	48,942 mol m^{-3}	
ω	Relaxation parameter	1.5	
σ_{GB}	Specific grain boundary conductivity of Al-LLZO	9.6×10^{-5} S m^{-1}	[60,62]
k_{pos}	Standard rate constant for positive electrode charge transfer reaction	5.1×10^{-6} m$^{2.8}$ mol$^{-0.6}$ s^{-1}	[44]
–	Theoretical density of Al-LLZO	5139 kg m^{-3}	[61]
–	Void conductivity	10^{-20} S m^{-1}	

[a] Base parameters unless otherwise specified.

To find the total voltage, the overpotential components are added to the equilibrium voltage [44]:

$$E_{bat} = E^{eq}_{bat} + \eta_{total} = E^{eq}_{LiCoO2} + \eta_d + \eta_{ct} + \eta_r \tag{26}$$

This grouping of overpotential components describes Nernst deviations from standard potentials, diffusion, and resistive effects within the battery system, while allowing the use of experimental tabulations of equilibrium voltages for increased accuracy. The simulation is stopped when the voltage reaches 0 or when the positive electrode surface at the interface with the electrolyte is fully lithiated, which causes a rapid increase in the magnitude of the diffusion overpotential.

The battery performance model was created in Python and validated by running parameters representative of a battery with a $LiCoO_2$ positive electrode, Li-metal negative electrode, and Li_3PO_4 electrolyte. The results were compared to previous computational and experimental results on solid-state batteries of this chemistry, and good agreement was found between the two to verify the validity of the governing equations [44].

A summary of the parameters used to model the behavior of Al-LLZO batteries is presented in Table 2. Uncited parameters are either chosen geometric parameters, based on material properties, or estimated. The Al-LLZO conductivity values were experimentally found in Ref. [60] at a stoichiometry of $Li_{6.55}Al_{0.15}La_3Zr_2O_{12}$. The initial activity of Li in the positive electrode is a chosen value, the initial activity of Li in the electrolyte is based on the molecular weight and theoretical density of Al-LLZO [61]. Voids are representative of pores, and the estimated void conductivity value is reflective of the null Li conductivity value of a pore. The specific grain boundary conductivity was calculated using Equation (27) [62] using $\sigma_{GB\ Total}$ data from Ref. [60].

$$\sigma_{GB} = \frac{L_{GB}}{L_{GI}}\sigma_{GB\ Total} \tag{27}$$

A summary of the equations used is represented in a flow chart in the Supplementary Information (Fig. S2).

3. Results

The effects of varying the electrolyte conductivity, thickness, grain size, grain boundary thickness, and void fraction on solid-state battery (SSB) performance are evaluated.

3.1. Discharge curves and overpotential components using battery performance model

In Fig. 3, discharge curves and overpotential components are shown for a battery simulated at a C-rate of 10, with the parameters specified in Table 1, and with a void fraction of 0. In Fig. 3a, the voltage as a function of specific capacity is shown, which can be used to calculate key battery performance properties such as energy and power output. In Fig. 3b, overpotential components can be individually observed. The diffusion overpotential is larger at the beginning and end of the battery life due to contributions from the positive electrode ($E^{eq}_{LiCoO_2}(x^s) - E^{eq}_{LiCoO_2}(\overline{x})$). $E^{eq}_{LiCoO_2}(x)$ decreases at a higher rate at lower lithiation values and at lithiation values close to one, which causes the difference between

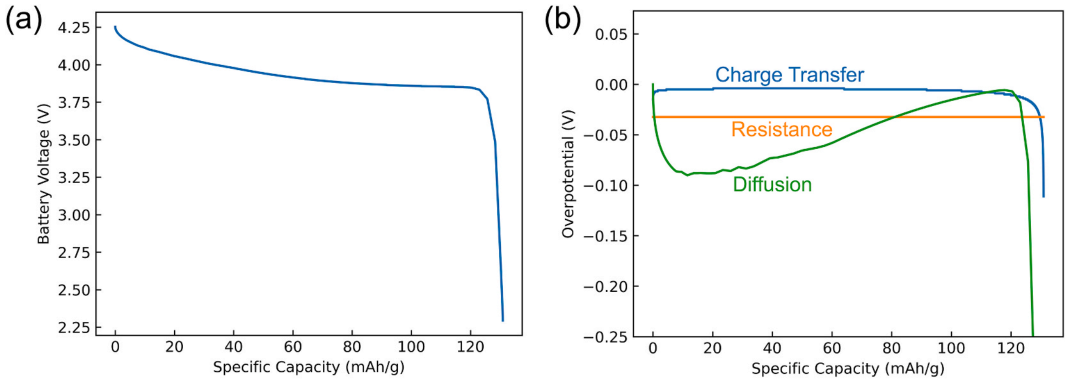

Fig. 3. (a) Voltage as a function of specific capacity during a discharge at a C-rate of 10. (b) Resistance, diffusion, and charge transfer overpotential components as a function of specific capacity during a discharge at a C-rate of 10. The positive electrode mass is 2.40×10^{-4} g.

$E^{eq}_{LiCoO_2}(x^s)$ and $E^{eq}_{LiCoO_2}(\overline{x})$ to be larger and increases the diffusion overpotential. Ultimately, diffusion overpotential is the cause of battery death in this example. At the end of the battery's life, all of the CoO_2 at the interface between the positive electrode and the electrolyte has reacted with Li ions to form $LiCoO_2$. This happens as a result of the diffusion through the positive electrode becoming slower than the rate of lithiation at this interface. The final diffusion overpotential value is -1.46 V. The charge-transfer overpotential also begins to contribute significantly as the battery dies, with a final value of -0.11 V. The resistance overpotential is relatively stable throughout discharge. The final resistance overpotential is -0.032 V. Fig. 3 demonstrates the ability of the simulation to provide detailed battery performance information.

3.2. Effects of electrolyte conductivity and thickness on SSB performance

In Fig. 4, the effects of conductivity normalized by electrolyte thickness—a proxy for electrolyte resistance—are shown over a range of electrolyte thicknesses at varying C-rates. Similar performance is obtained for batteries with different electrolyte conductivities or thicknesses, but with the same ratio of the two. Modeling of battery performance is performed for electrolytes with conductivities between 9.6×10^{-7} S cm^{-1} and 7.2×10^{-4} S cm^{-1} and thicknesses between 1 μm and 100 μm. The conductivity range was chosen to span a wide range of possible conductivity values as grain boundary thickness and grain size are varied (consistent with the span of conductivity values in Fig. 5a). As expected, higher overpotentials are seen as conductivity decreases and electrolyte thickness increases, leading to lower energy and power values. Below a ratio of 10 S m^{-2}, the energy and power values drop off, particularly at higher C-rates, with steep energy output decreases at a C-rate of 10 and effectively no energy output at a C-rate of 100.

3.3. Effect of grain size on SSB performance

Fig. 5a demonstrates the effect of grain size on conductivity and diffusion coefficient as grain size is varied between 0.1 nm and 0.1 mm with a constant grain boundary thickness of 7.5 nm. As expected, due to higher conductivity in the grain interior than the grain boundary, increases in grain size at constant grain boundary thickness result in increased overall conductivity and diffusion coefficients until they approach that of the grain interior. The change in conductivity occurs primarily between grain sizes of 10 nm and 10 μm, or when the ratio of grain size to grain boundary thickness is between 1 and 10^3. Below grain sizes of 10 nm, the conductivity asymptotes towards the grain boundary conductivity (9.6×10^{-7} S cm^{-1}) as the grain boundary, which encases each grain interior, becomes the main pathway for Li ions. Above grain sizes of 75 μm, or above a ratio of grain size to grain boundary of 10^4, the conductivity slowly approaches the grain interior conductivity, reaching 92.6% of its 7.7×10^{-4} S cm^{-1} value. Because the grain boundary fully encases each grain, forcing Li ions to travel through the grain boundary, it requires much larger grain sizes than grain boundaries for the overall conductivity to approach the grain interior conductivity.

The diffusion coefficients in Fig. 5a are then used as model parameters to determine the overall battery performance for different grain sizes. This is shown in Fig. 5b, which provides the fraction of the theoretical energy output of the battery at different C-rates and grain sizes. The theoretical output is determined by multiplying the theoretical capacity of $LiCoO_2$, the mass of the active material in the positive electrode, and the average equilibrium voltage over the range of lithiation modeled. The theoretical energy output is 149 μW*hr when starting

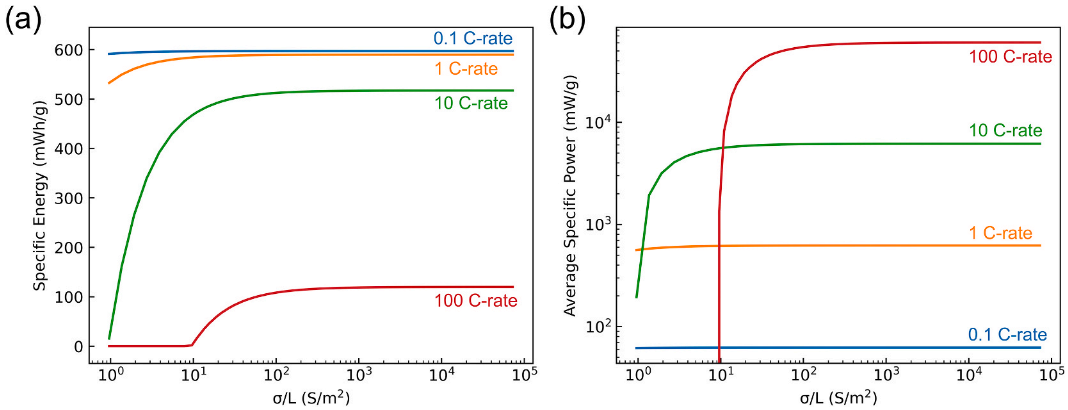

Fig. 4. (a) Specific energy output of the battery as a function of the ratio of electrolyte conductivity to thickness. (b) Specific average power output of the battery as a function of the ratio of electrolyte conductivity to thickness. The positive electrode mass is 2.40×10^{-4} g.

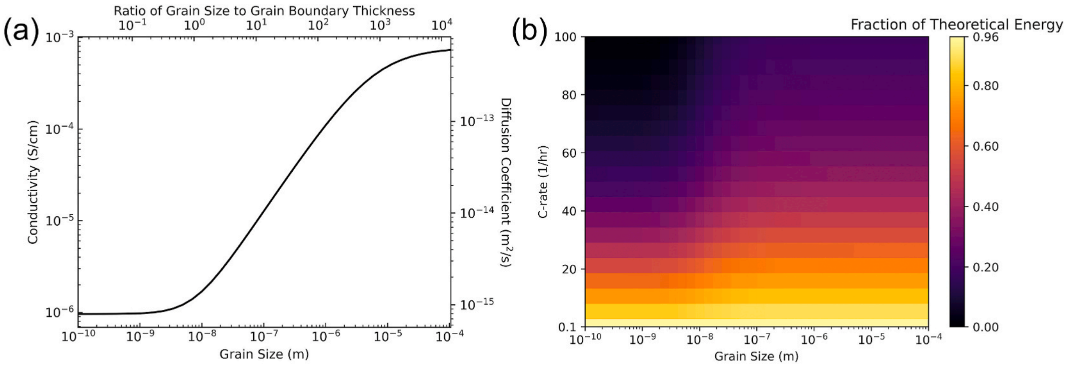

Fig. 5. (a) Conductivity and diffusion coefficient as a function of grain size and ratio of grain size to grain boundary thickness. (b) Fraction of theoretical energy obtained as a function of C-rate and grain size.

with a 43% initial lithiation in the positive electrode (corresponding to a specific capacity of 156 mAh g^{-1} that is 57% of the full 274 mAh g^{-1} for the positive electrode). The C-rate represents the theoretical C-rate based on the applied current, calculated using:

$$C-rate = \frac{I}{Q_{theoretical}} \tag{28}$$

Where $Q_{theoretical}$ is the theoretical capacity of the $LiCoO_2$ electrode based on the amount of active material and taking into consideration the initial lithiation of the positive electrode.

In Fig. 5b, increased grain size and decreased C-rates lead to higher energy outputs. The maximum fraction of theoretical energy output is 0.96, achieved at a C-rate of 0.1 and a grain size of 0.1 mm. Additionally, the specific capacity at this C-rate was found to be 150 mAh g^{-1} over the range of grain sizes, which is comparable to experimental results with thin-film LLZO/$LiCoO_2$ batteries [36]. At higher C-rates, lower capacities are achieved. For example, at C-rates of 100, 52.7, and 5.4, the battery capacities are 30.8 mAh g^{-1}, 58.7 mAh g^{-1}, and 140 mAh g^{-1}, respectively. The limitations of the positive electrode kinetics are a large contributor to these differences. Overall, there is a significant decrease in energy output at grain sizes smaller than 10 nm and above C-rates of 50 where the battery energy output becomes extremely small (approaching 0). However, the grain size has significant effects at lower C-rates as well: at a C-rate of 10.6, the fraction of theoretical energy ranges between 0.739 and 0.825, representing a 0.086 difference in fraction energy output. If the grain size is kept above 100 nm, most of these effects can be mitigated. This indicates that for systems like Al-LLZO, where the grain boundary conductivity is significantly lower than that of the bulk, it is important that the grain size must be ~10 times larger than the grain boundary thickness, with more importance on increasing this ratio at higher C-rates.

3.4. Effect of electrolyte grain boundary thickness on SSB performance

Fig. 6a shows the effect of grain boundary thickness on conductivity and diffusion coefficient as grain boundary thickness is varied between 0.1 nm and 4 μm, while the grain size is 100 nm. Similar to the effects seen when varying grain size, the higher conductivity of the grain interior causes a decrease in conductivity and diffusion as grain boundary thickness increases. Above a grain boundary thickness of 100 nm, the conductivity approaches the grain boundary conductivity (9.6×10^{-7} S cm^{-1}). The grain boundary thickness values do not get small enough to cause the overall conductivity to begin to plateau towards the grain interior conductivity, as the grain boundary has a stronger impact on the overall conductivity due to the current always having to travel through the boundary.

In Fig. 6b, the simulated fraction of theoretical energy output at varying grain boundary thicknesses and C-rates is shown. It is observed that decreases in both C-rate and grain boundary thickness lead to increased energy output, which is consistent with theory. The maximum fraction of energy output is again 0.96. There is a transition above a C-rate of ~40 and a grain boundary thickness of ~30 nm where energy output becomes very small. The negative battery performance effects are minimal when the grain boundary thickness is below 10 nm.

3.5. Effect of electrolyte voids on SSB performance

In Fig. 7a, the effects of the void fraction of the LLZO electrolyte on the overall conductivity and diffusion coefficient are shown. The void fraction quantifies the area fraction of voids in the electrolyte and is representative of the effects of porosity on solid electrolytes. The simulation was run with a grain size of 100 nm and a grain boundary thickness of 7.5 nm. The void fraction was varied by placing randomly spaced voids within the resistor network matrix, leading to the

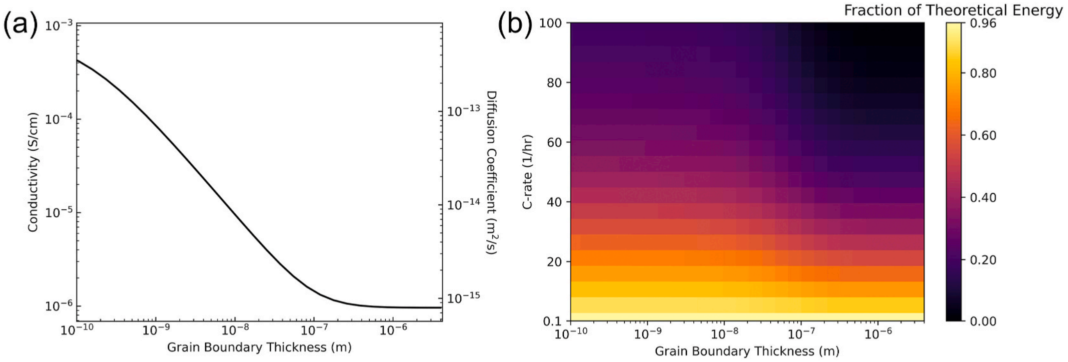

Fig. 6. (a) Conductivity and diffusion coefficient as a function of grain boundary thickness. (b) Fraction of theoretical energy obtained as a function of C-rate and grain boundary thickness.

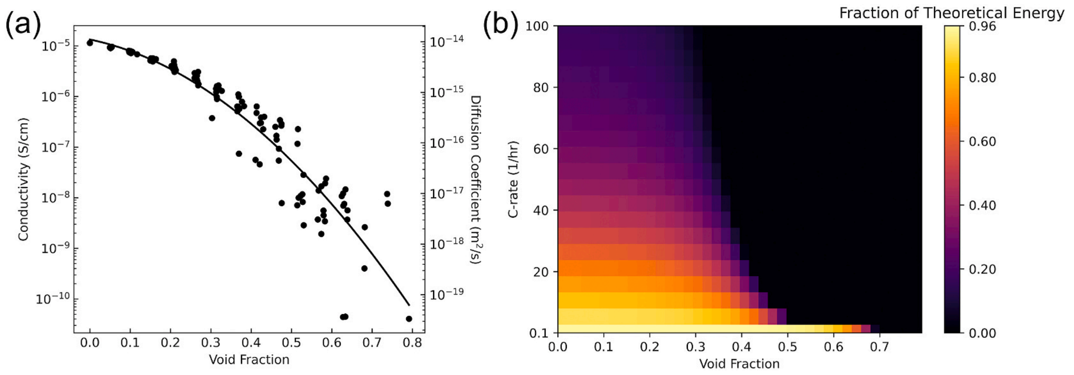

Fig. 7. (a) Conductivity and diffusion coefficient as a function of void fraction. The line is a quadratic fit used to approximate the log of conductivity as a function of void fraction. (b) Fraction of theoretical energy obtained as a function of C-rate and void fraction.

variability in conductivity and diffusion coefficient seen in Fig. 7a. As the void fraction decreases to 0, the conductivity and diffusion coefficient increase towards the conductivity of an Al-LLZO electrolyte with grain size of 0.1 μm, a grain boundary thickness of 7.5 nm, and no voids: 1.145×10^{-5} S cm^{-1}. Above a void fraction density of ~0.8, the conductivity quickly drops to 0. Similar trends of increasing conductivity as relative density and porosity increases in LLZO have been seen experimentally, though the effects of porosity were unable to be disentangled from effects of grain size and grain boundary chemistry [24,63].

In Fig. 7b, the values of diffusion coefficients for varying void fractions are used to determine battery performance characteristics. At high void fractions and high C-rates, the battery produces negligible energy output due to the extremely high overpotentials in the electrolyte. To avoid major battery performance losses, the void fraction must stay below ~0.3. At lower C-rates, the battery is able to operate at higher void fractions—at very low C-rates the battery can perform at void fractions up to 0.6. At void fractions below 0.1, minimal losses are seen due to ionic conductivity of the electrolyte.

4. Discussion

The battery performance model results suggest that a ratio of electrolyte conductivity to thickness should remain above 10 S m^{-2} for high performance, particularly at higher C-rates above 10. Incorporating the resistor network model, results suggest that energy output losses due to microstructure features can be minimized with grain sizes larger than 100 nm for a grain boundary thickness of 7.5 nm, grain boundaries smaller than 10 nm for a grain size of 100 nm, and void fractions below 0.1 for a grain size of 100 nm and a grain boundary thickness of 7.5 nm. Experimentally, LLZO grain boundary thicknesses in the range of 2–7.5 nm have been observed [23], grain sizes of 100 nm have been measured in thin films [35], and high relatively densities up to 99% suggesting low void fraction have been observed [24]. Current electrolyte properties are already able to meet or exceed the microstructure design parameters suggested. Even at C-rates up to 100, further improvement of the electrolyte microstructure provides diminishing returns in energy output. This is important to note as faster charging comes into focus as an important next step for use in electric vehicles and other personal devices.

Overall, the model combines a resistor network model and a finite difference method-based battery performance model to evaluate the effect of solid-state electrolyte microstructure on battery performance, allowing for unique insight into the significance of electrolyte microstructure properties. Some of the limitations of the model include limited geometries due to the grid-shaped resistor network model, assumptions of constant $LiCoO_2$ diffusion coefficient at different lithiation levels, and the one-dimensional nature of the battery performance model. The specific results presented here have also not yet been experimentally validated, though both the battery performance model and the resistor network model have been validated independently [42,44]. To the author's knowledge, there has not been a systematic experimental study, of this type, on the effect of electrolyte microstructure properties on battery performance. Additionally, there are several interconnected ways electrolyte microstructure affects battery performance that are not explored here, which include the effect of grain boundaries and pore networks on dendrite formation [64], high interfacial resistances caused by secondary phase formation or poor connectivity [36,65,66], and the ways in which microstructure affects the stability of Al-LLZO [66]. Some of these effects, along with electrode kinetics, have been suggested as more critical limiting factors of solid-state batteries than the improvement of electrolyte conductivity [2,66]. This is consistent with the results seen for Al-LLZO, which show that further refinement of electrolyte microstructure is unlikely to significantly improve performance. However, this is not necessarily the case for other solid-state electrolyte chemistries and similar studies would need to be carried out to determine the effect of microstructure on battery performance in those cases.

The values of the initial fraction of mobile lithium (δ) and the mobile Li ion recombination rate (k_r) in LLZO are not well established. Hayamizu et al. and Buschmann et al. have studied the quantities of mobile Li ions in LLZO and Al-LLZO respectively, but the value of δ at room temperature has not been experimentally determined for any LLZO [8,67]. No experimental values for k_r have been found. In other work [44,45,49], these parameters were determined through curve fitting to experimental data. However, both δ and k_r were found to have minimal effects on total energy output. The effect of these parameters is shown in the Supplementary Information (Fig. S3 and Fig. S4).

5. Conclusion

A continuum, one-dimensional, finite-difference battery performance model was used in combination with a resistor network model to determine solid electrolyte microstructure effects on battery performance. Energy output results were comparable to experimental results from other papers. Regardless of electrolyte conductivity, ratios of electrolyte conductivity to electrolyte thickness above 10 S m^{-2} are necessary to facilitate good battery performance at C-rates above 10, with larger performance gains at higher C-rates. The resistor network model predicts that as grain sizes increase, the Al-LLZO bulk electrolyte conductivity will approach the higher grain interior conductivity, estimated to reach 92.6% of that value for grain sizes at least 10,000 times larger than grain boundary thicknesses. Negative battery performance effects due to electrolyte microstructure were minimal for Al-LLZO electrolytes with grain sizes larger than 100 nm for a grain boundary thickness of 7.5 nm, grain boundaries smaller than 10 nm for a grain size of 100 nm, and void fractions below 0.1 for a grain size of 100 nm and a grain boundary thickness of 7.5 nm. Current Al-LLZO electrolytes are already able to meet these criteria, and simulations predict minimal battery performance improvements through microstructures more optimized for high conductivity, even up to C-rates as high as 100. Future work includes the addition of different and irregular microstructure geometries, the inclusion of additional interfacial resistance phenomena, dendrite formation modeling, and modeling of chemical stability and particle degradation. Additionally, by applying this model to different battery chemistries and solid electrolytes, different design rules and optimal microstructures tailored for specific systems can be explored. This could be particularly useful for less conductive solid electrolytes, where microstructure optimization may have a large impact on battery performance.

CRediT authorship contribution statement

Maya Horii: Conceptualization, Methodology, Software, Validation, Writing – original draft, Writing – review & editing. **Rebecca J. Christianson:** Conceptualization, Software, Validation, Writing – review & editing. **Heena Mutha:** Conceptualization, Software, Validation, Writing – review & editing. **John Christopher Bachman:** Conceptualization, Writing – review & editing, Funding acquisition, Supervision, Project administration.

Declaration of competing interest

The authors declare that they have no known competing financial interests or personal relationships that could have appeared to influence the work reported in this paper.

Acknowledgements

This work was supported by the Cal State LA Partnership for Research and Education in Materials; the National Science Foundation (No. DMR-1523588); and The Charles Stark Draper Laboratory.

Appendix A. Supplementary data

Supplementary data to this article can be found online at https://doi.org/10.1016/j.jpowsour.2022.231177.

References

[1] F. Zheng, M. Kotobuki, S. Song, M.O. Lai, L. Lu, Review on solid electrolytes for all-solid-state lithium-ion batteries, J. Power Sources 389 (Jun. 2018) 198–213, https://doi.org/10.1016/j.jpowsour.2018.04.022.

[2] A.C. Luntz, J. Voss, K. Reuter, Interfacial challenges in solid-state Li ion batteries, J. Phys. Chem. Lett. 6 (22) (2015) 4599–4604, https://doi.org/10.1021/acs.jpclett.5b02352. Nov.

[3] M.V. Reddy, C.M. Julien, A. Mauger, K. Zaghib, Sulfide and oxide inorganic solid electrolytes for all-solid-state Li batteries: a review, Nanomaterials 10 (8) (Aug. 2020) 1606, https://doi.org/10.3390/nano10081606.

[4] V. Thangadurai, S. Narayanan, D. Pinzaru, Garnet-type solid-state fast Li ion conductors for Li batteries: critical review, Chem. Soc. Rev. 43 (13) (2014) 4714, https://doi.org/10.1039/c4cs00020j.

[5] Q. Liu, et al., Challenges and perspectives of garnet solid electrolytes for all solid-state lithium batteries, J. Power Sources 389 (2018) 120–134, https://doi.org/10.1016/j.jpowsour.2018.04.019. Jun.

[6] R. Murugan, V. Thangadurai, W. Weppner, Fast lithium ion conduction in garnet-type Li7La3Zr2O12, Angew. Chem. Int. Ed. 46 (41) (Oct. 2007) 7778–7781, https://doi.org/10.1002/anie.200701144.

[7] W. Lu, M. Xue, C. Zhang, Modified Li7La3Zr2O12 (LLZO) and LLZO-polymer composites for solid-state lithium batteries, Energy Storage Mater. 39 (Aug. 2021) 108–129, https://doi.org/10.1016/j.ensm.2021.04.016.

[8] H. Buschmann, et al., Structure and dynamics of the fast lithium ion conductor ‘Li7La3Zr2O12, Phys. Chem. Chem. Phys. 13 (43) (2011), https://doi.org/10.1039/c1cp22108f, 19378.

[9] A. Moradabadi, P. Kaghazchi, Defect chemistry in cubic Li6.25Al0.25La3Zr2O12 solid electrolyte: a density functional theory study, Solid State Ionics 338 (Oct. 2019) 74–79, https://doi.org/10.1016/j.ssi.2019.04.023.

[10] X. Shen, et al., Critical challenges and progress of solid garnet electrolytes for all-solid-state batteries, Mater. Today Chem. 18 (Dec. 2020) 100368, https://doi.org/10.1016/j.mtchem.2020.100368.

[11] B. Karasulu, S.P. Emge, M.F. Groh, C.P. Grey, A.J. Morris, Al/Ga-Doped $Li_7La_3Zr_2O_{12}$ garnets as Li-ion solid-state battery electrolytes: atomistic insights into local coordination environments and their influence on ^{17}O, ^{27}Al, and ^{71}Ga NMR spectra, J. Am. Chem. Soc. 142 (6) (2020) 3132–3148, https://doi.org/10.1021/jacs.9b12685. Feb.

[12] Y. Jin, P.J. McGinn, Al-doped Li7La3Zr2O12 synthesized by a polymerized complex method, J. Power Sources 196 (20) (Oct. 2011) 8683–8687, https://doi.org/10.1016/j.jpowsour.2011.05.065.

[13] F. Liang, Y. Sun, Y. Yuan, J. Huang, M. Hou, J. Lu, Designing inorganic electrolytes for solid-state Li-ion batteries: a perspective of LGPS and garnet, Mater. Today (Apr. 2021), https://doi.org/10.1016/j.mattod.2021.03.013. S1369702121001073.

[14] X. Ke, Y. Wang, L. Dai, C. Yuan, Cell failures of all-solid-state lithium metal batteries with inorganic solid electrolytes: lithium dendrites, Energy Storage Mater. 33 (Dec. 2020) 309–328, https://doi.org/10.1016/j.ensm.2020.07.024.

[15] F. Han, et al., High electronic conductivity as the origin of lithium dendrite formation within solid electrolytes, Nat. Energy 4 (3) (2019) 187–196, https://doi.org/10.1038/s41560-018-0312-z. Mar.

[16] W. Guo, et al., In-situ optical observation of Li growth in garnet-type solid state electrolyte, Energy Storage Mater. 41 (2021) 791–797, https://doi.org/10.1016/j.ensm.2021.07.023. Oct.

[17] K. Kerman, A. Luntz, V. Viswanathan, Y.-M. Chiang, Z. Chen, Review—practical challenges hindering the development of solid state Li ion batteries, J. Electrochem. Soc. 164 (7) (2017) A1731–A1744, https://doi.org/10.1149/2.1571707jes.

[18] H. Wang, L. Sheng, G. Yasin, L. Wang, H. Xu, X. He, Reviewing the current status and development of polymer electrolytes for solid-state lithium batteries, Energy Storage Mater. 33 (Dec. 2020) 188–215, https://doi.org/10.1016/j.ensm.2020.08.014.

[19] Y. Liu, et al., Insight into the microstructure and ionic conductivity of cold sintered NASICON solid electrolyte for solid-state batteries, ACS Appl. Mater. Interfaces 11 (31) (Aug. 2019) 27890–27896, https://doi.org/10.1021/acsami.9b08132.

[20] L. Cheng, et al., Effect of surface microstructure on electrochemical performance of garnet solid electrolytes, ACS Appl. Mater. Interfaces 7 (3) (2015) 2073–2081, https://doi.org/10.1021/am508111r. Jan.

[21] Y. Zhang, et al., Influence of chemical microstructure of single-ion polymeric electrolyte membranes on performance of lithium-ion batteries, ACS Appl. Mater. Interfaces 6 (20) (Oct. 2014) 17534–17542, https://doi.org/10.1021/am503152m.

[22] Y. Zhu, S. Wu, Y. Pan, X. Zhang, Z. Yan, Y. Xiang, Reduced energy barrier for Li+ transport across grain boundaries with amorphous domains in LLZO thin films, Nanoscale Res. Lett. 15 (1) (Dec. 2020) 153, https://doi.org/10.1186/s11671-020-03378-x.

[23] W.E. Tenhaeff, et al., Resolving the grain boundary and lattice impedance of hot-pressed $Li_7La_3Zr_2O_{12}$ garnet electrolytes, Chemelectrochem 1 (2) (Feb. 2014) 375–378, https://doi.org/10.1002/celc.201300022.

[24] I.N. David, T. Thompson, J. Wolfenstine, J.L. Allen, J. Sakamoto, Microstructure and Li-ion conductivity of hot-pressed cubic $Li_7La_3Zr_2O_{12}$, J. Am. Ceram. Soc. 98 (4) (Apr. 2015) 1209–1214, https://doi.org/10.1111/jace.13455.

[25] S. Teng, J. Tan, A. Tiwari, Recent developments in garnet based solid state electrolytes for thin film batteries, Curr. Opin. Solid State Mater. Sci. 18 (1) (Feb. 2014) 29–38, https://doi.org/10.1016/j.cossms.2013.10.002.

[26] S. Cao, et al., Modeling, preparation, and elemental doping of Li7La3Zr2O12 garnet-type solid electrolytes: a review, J. Kor. Ceram. Soc. 56 (2) (Mar. 2019) 111–129, https://doi.org/10.4191/kcers.2019.56.2.01.

[27] L. Cheng, et al., Effect of microstructure and surface impurity segregation on the electrical and electrochemical properties of dense Al-substituted $Li_7La_3Zr_2O_{12}$, J. Mater. Chem. A 2 (1) (2014) 172–181, https://doi.org/10.1039/C3TA13999A.

[28] J. Wolfenstine, J. Sakamoto, J.L. Allen, Electron microscopy characterization of hot-pressed Al substituted Li7La3Zr2O12, J. Mater. Sci. 47 (10) (May 2012) 4428–4431, https://doi.org/10.1007/s10853-012-6300-y.

[29] E. Rangasamy, J. Wolfenstine, J. Sakamoto, The role of Al and Li concentration on the formation of cubic garnet solid electrolyte of nominal composition Li7La3Zr2O12, Solid State Ionics 206 (Jan. 2012) 28–32, https://doi.org/10.1016/j.ssi.2011.10.022.

[30] P.R. Cantwell, M. Tang, S.J. Dillon, J. Luo, G.S. Rohrer, M.P. Harmer, Grain boundary complexions, Acta Mater. 62 (Jan. 2014) 1–48, https://doi.org/10.1016/j.actamat.2013.07.037.

[31] Y. Zhang, F. Chen, R. Tu, Q. Shen, L. Zhang, Field assisted sintering of dense Al-substituted cubic phase Li7La3Zr2O12 solid electrolytes, J. Power Sources 268 (Dec. 2014) 960–964, https://doi.org/10.1016/j.jpowsour.2014.03.148.

[32] Y. Zhang, D. Luo, W. Luo, S. Du, Y. Deng, J. Deng, High-purity and high-density cubic phase of Li7La3Zr2O12 solid electrolytes by controlling surface/volume ratio and sintering pressure, Electrochim. Acta 359 (Nov. 2020) 136965, https://doi.org/10.1016/j.electacta.2020.136965.

[33] K.B. Dermenci, E. Çekiç, S. Turan, Al stabilized Li7La3Zr2O12 solid electrolytes for all-solid state Li-ion batteries, Int. J. Hydrogen Energy 41 (23) (Jun. 2016) 9860–9867, https://doi.org/10.1016/j.ijhydene.2016.03.197.

[34] R. Pfenninger, M. Struzik, I. Garbayo, E. Stilp, J.L.M. Rupp, A low ride on processing temperature for fast lithium conduction in garnet solid-state battery films, Nat. Energy 4 (6) (Jun. 2019) 475–483, https://doi.org/10.1038/s41560-019-0384-4.

[35] J. Tan, A. Tiwari, Fabrication and characterization of Li7La3Zr2O12 thin films for lithium ion battery, ECS Solid State Lett. 1 (6) (Oct. 2012), https://doi.org/10.1149/2.013206ssl. Q57–Q60.

[36] J. Sastre, X. Chen, A. Aribia, A.N. Tiwari, Y.E. Romanyuk, Fast charge transfer across the $Li_7La_3Zr_2O_{12}$ solid electrolyte/$LiCoO_2$ cathode interface enabled by an interphase-engineered all-thin-film architecture, ACS Appl. Mater. Interfaces 12 (32) (Aug. 2020) 36196–36207, https://doi.org/10.1021/acsami.0c09777.

[37] A.J. Samson, K. Hofstetter, S. Bag, V. Thangadurai, A bird's-eye view of Li-stuffed garnet-type $Li_7La_3Zr_2O_{12}$ ceramic electrolytes for advanced all-solid-state Li batteries, Energy Environ. Sci. 12 (10) (2019) 2957–2975, https://doi.org/10.1039/C9EE01548E.

[38] W. Li, Y. Ando, E. Minamitani, S. Watanabe, Study of Li atom diffusion in amorphous Li3PO4 with neural network potential, J. Chem. Phys. 147 (21) (Dec. 2017) 214106, https://doi.org/10.1063/1.4997242.

[39] K.-S. Chang, Y.-F. Lin, K.-L. Tung, Insight into the grain boundary effect on the ionic transport of yttria-stabilized zirconia at elevated temperatures from a molecular modeling perspective, J. Power Sources 196 (22) (Nov. 2011) 9322–9330, https://doi.org/10.1016/j.jpowsour.2011.07.085.

[40] J.A. Dawson, P. Canepa, T. Famprikis, C. Masquelier, M.S. Islam, Atomic-scale influence of grain boundaries on Li-ion conduction in solid electrolytes for all-solid-state batteries, J. Am. Chem. Soc. 140 (1) (Jan. 2018) 362–368, https://doi.org/10.1021/jacs.7b10593.

[41] S. Yu, D.J. Siegel, Grain boundary contributions to Li-ion transport in the solid electrolyte $Li_7La_3Zr_2O_{12}$ (LLZO), Chem. Mater. 29 (22) (Nov. 2017) 9639–9647, https://doi.org/10.1021/acs.chemmater.7b02805.

[42] O. Birkholz, Y. Gan, M. Kamlah, Modeling the effective conductivity of the solid and the pore phase in granular materials using resistor networks, Powder Technol. 351 (Jun. 2019) 54–65, https://doi.org/10.1016/j.powtec.2019.04.005.

[43] S. Han, J. Park, W. Lu, A.M. Sastry, Numerical study of grain boundary effect on Li + effective diffusivity and intercalation-induced stresses in Li-ion battery active materials, J. Power Sources 240 (Oct. 2013) 155–167, https://doi.org/10.1016/j.jpowsour.2013.03.135.

[44] D. Danilov, R.A.H. Niessen, P.H.L. Notten, Modeling all-solid-state Li-ion batteries, J. Electrochem. Soc. 158 (3) (2011) A215, https://doi.org/10.1149/1.3521414.

[45] A. Bates, S. Mukherjee, N. Schuppert, B. Son, J.G. Kim, S. Park, Modeling and simulation of 2D lithium-ion solid state battery: effects of materials and geometry on the performance of SSB, Int. J. Energy Res. 39 (11) (Sep. 2015) 1505–1518, https://doi.org/10.1002/er.3344.

[46] S. Gantenbein, M. Weiss, E. Ivers-Tiffée, Impedance based time-domain modeling of lithium-ion batteries: Part I, J. Power Sources 379 (Mar. 2018) 317–327, https://doi.org/10.1016/j.jpowsour.2018.01.043.

[47] S.S. Sandhu, J.P. Fellner, Model formulation and simulation of a solid-state lithium-based cell, Electrochim. Acta 88 (Jan. 2013) 495–506, https://doi.org/10.1016/j.electacta.2012.10.110.

[48] L.H.J. Raijmakers, D.L. Danilov, R.-A. Eichel, P.H.L. Notten, An advanced all-solid-state Li-ion battery model, Electrochim. Acta 330 (Jan. 2020) 135147, https://doi.org/10.1016/j.electacta.2019.135147.

[49] N. Kazemi, D.L. Danilov, L. Haverkate, N.J. Dudney, S. Unnikrishnan, P.H. L. Notten, Modeling of all-solid-state thin-film Li-ion batteries: accuracy improvement, Solid State Ionics 334 (Jun. 2019) 111–116, https://doi.org/10.1016/j.ssi.2019.02.003.

[50] S.D. Fabre, D. Guy-Bouyssou, P. Bouillon, F. Le Cras, C. Delacourt, Charge/discharge simulation of an all-solid-state thin-film battery using a one-dimensional model, J. Electrochem. Soc. 159 (2) (2011), https://doi.org/10.1149/2.041202jes. A104–A115.

[51] E. Barsoukov, J.R. Macdonald (Eds.), Impedance Spectroscopy: Theory, Experiment, and Applications, second ed., Wiley-Interscience, Hoboken, N.J, 2005.

[52] J. Fleig, The influence of non-ideal microstructures on the analysis of grain boundary impedances, Solid State Ionics 131 (1–2) (Jun. 2000) 117–127, https://doi.org/10.1016/S0167-2738(00)00627-5.

[53] J. Fleig, The grain boundary impedance of random microstructures: numerical simulations and implications for the analysis of experimental data, Solid State Ionics 150 (1–2) (Sep. 2002) 181–193, https://doi.org/10.1016/S0167-2738(02)00274-6.

[54] Y. Yuge, Three-dimensional site percolation problem and effective-medium theory: a computer study, J. Stat. Phys. 16 (4) (Apr. 1977) 339–348, https://doi.org/10.1007/BF01020426.

[55] S. Kirkpatrick, Classical transport in disordered media: scaling and effective-medium theories, Phys. Rev. Lett. 27 (25) (Dec. 1971) 1722–1725, https://doi.org/10.1103/PhysRevLett.27.1722.

[56] S. Mittal, "A Study of Successive Over-relaxation (SOR) Method Parallelization over Modern HPC Languages," p. 6.

[57] A. Dorai, N. Kuwata, R. Takekawa, J. Kawamura, K. Kataoka, J. Akimoto, Diffusion coefficient of lithium ions in garnet-type Li6.5La3Zr1.5Ta0.5O12 single crystal probed by 7Li pulsed field gradient-NMR spectroscopy, Solid State Ionics 327 (Dec. 2018) 18–26, https://doi.org/10.1016/j.ssi.2018.10.016.

[58] M. Chintapalli, et al., Relationship between conductivity, ion diffusion, and transference number in perfluoropolyether electrolytes, Macromolecules 49 (9) (May 2016) 3508–3515, https://doi.org/10.1021/acs.macromol.6b00412.

[59] All-Solid-State Lithium-Ion Battery." COMSOL.

[60] F.M. Pesci, R.H. Brugge, A.K.O. Hekselman, A. Cavallaro, R.J. Chater, A. Aguadero, Elucidating the role of dopants in the critical current density for dendrite formation in garnet electrolytes, J. Mater. Chem. A 6 (40) (2018) 19817–19827, https://doi.org/10.1039/C8TA08366E.

[61] S. Yu, et al., Elastic properties of the solid electrolyte $Li_7La_3Zr_2O_{12}$ (LLZO), Chem. Mater. 28 (1) (Jan. 2016) 197–206, https://doi.org/10.1021/acs.chemmater.5b03854.

[62] M. Martin, Grain boundary ionic conductivity of yttrium stabilized zirconia as a function of silica content and grain size, Solid State Ionics 161 (1–2) (Jul. 2003) 67–79, https://doi.org/10.1016/S0167-2738(03)00265-0.

[63] Y. Kim, H. Jo, J.L. Allen, H. Choe, J. Wolfenstine, J. Sakamoto, The effect of relative density on the mechanical properties of hot-pressed cubic $Li_7La_3Zr_2O_{12}$, J. Am. Ceram. Soc. 99 (4) (Apr. 2016) 1367–1374, https://doi.org/10.1111/jace.14084.

[64] F. Shen, M.B. Dixit, X. Xiao, K.B. Hatzell, Effect of pore connectivity on Li dendrite propagation within LLZO electrolytes observed with synchrotron X-ray tomography, ACS Energy Lett. 3 (4) (Apr. 2018) 1056–1061, https://doi.org/10.1021/acsenergylett.8b00249.

[65] K. Park, et al., Electrochemical nature of the cathode interface for a solid-state lithium-ion battery: interface between $LiCoO_2$ and garnet-$Li_7La_3Zr_2O_{12}$, Chem. Mater. 28 (21) (Nov. 2016) 8051–8059, https://doi.org/10.1021/acs.chemmater.6b03870.

[66] L. Cheng, et al., Interrelationships among grain size, surface composition, air stability, and interfacial resistance of Al-substituted $Li_7La_3Zr_2O_{12}$ solid electrolytes, ACS Appl. Mater. Interfaces 7 (32) (Aug. 2015) 17649–17655, https://doi.org/10.1021/acsami.5b02528.

[67] K. Hayamizu, S. Seki, T. Haishi, Lithium ion micrometer diffusion in a garnet-type cubic $Li_7La_3Zr_2O_{12}$ (LLZO) studied using ^{7}Li NMR spectroscopy, J. Chem. Phys. 146 (2) (Jan. 2017) 24701, https://doi.org/10.1063/1.4973827.